Electronic Supplementary Material (ESI) for Chemical Science.

Supplemental information to *How the AI-assisted discovery and synthesis of a ternary oxide highlights capability gaps in materials science*

Joseph Montoya[‡,1,*], Carolyn Grimley[‡,2], Muratahan Aykol[1], Colin Ophus[3], Hadas Sternlicht[3,4], Benjamin H. Savitzky[3], Andrew M. Minor[3,4], Steven Torrisi[1], Jackson Goedjen[5], Ching-Chang Chung[2], Andrew Comstock[5], Shijing Sun[1]

‡ these authors contributed equally to this manuscript
** joseph.montoya@tri.global*

[1]Toyota Research Institute, Energy and Materials Division, Accelerated Materials Design and Discovery
[2]Lucideon, Inc.
[3]National Center for Electron Microscopy (NCEM), Molecular Foundry, Lawrence Berkeley Lab
[4]Department of Materials Science and Engineering, University of California, Berkeley
[5]North Carolina State University, Department of Physics

Ternary oxides reported from the ICSD over time

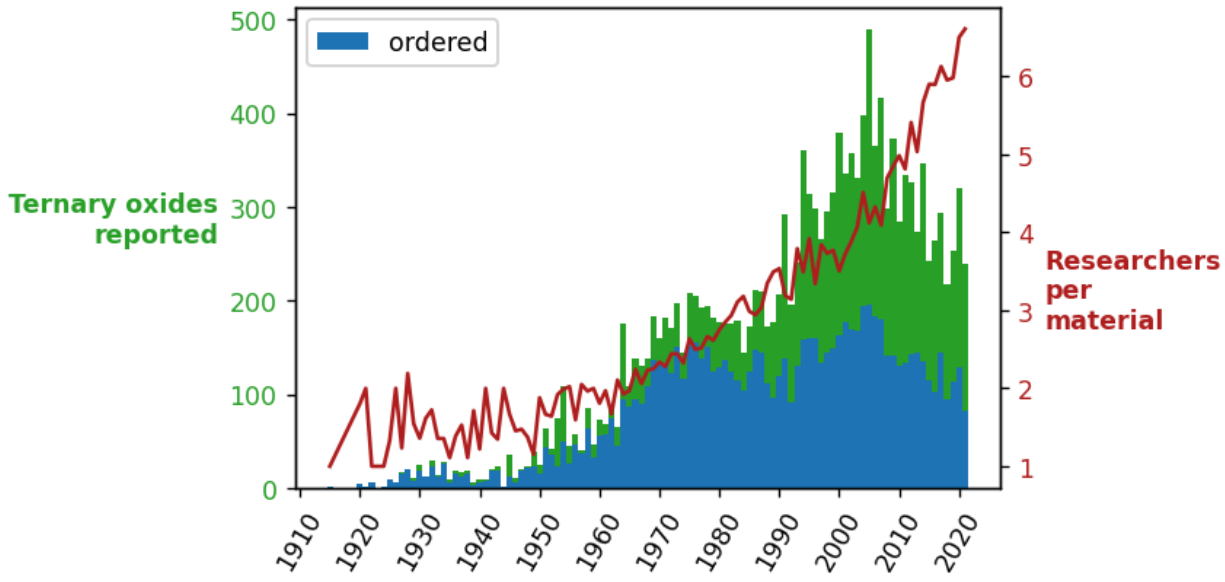

Figure S1: Ternary oxides reported in the ICSD by publication (i.e. associated citation) date. The blue region denotes ordered structures, and the green denotes disordered structures. The red line indicates the number of distinct authors in a given year divided by the number of crystal structures reported. Crystal structure data is deduplicated using pymatgen's StructureMatcher algorithm in order to ensure only distinct crystal structures are included. We note in the main text that following ~2005, the rate of discovery

of ternary oxides, both ordered (meaning no partial occupancies) and disordered (having at least one site with partial occupancies) have decreased.

Details of synthesis down selection

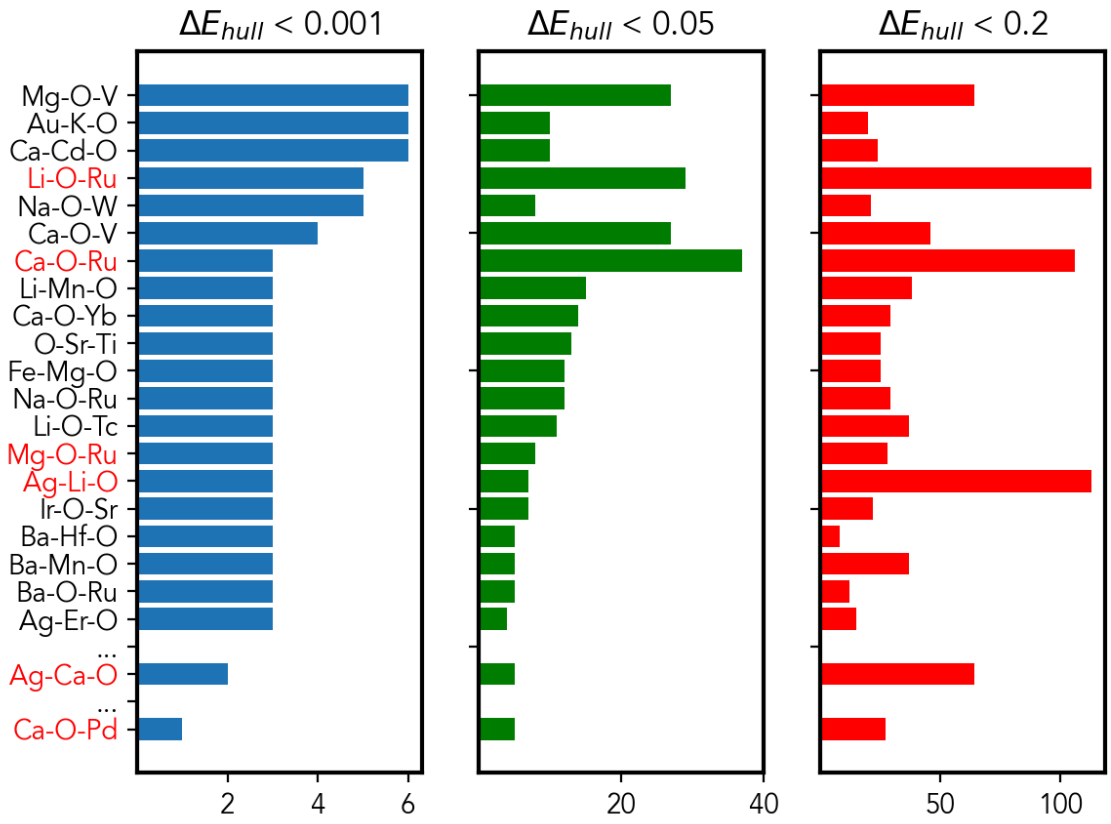

Figure S2: Selected ternary oxide chemical systems with the number of ground states (ΔE_{hull} < 0.001 eV/atom), near stable (ΔE_{hull} < 0.05 eV/atom), and metastable (ΔE_{hull} < 0.2 eV/atom), sorted by number of ground states. Chemical systems selected for synthesis in this work are shown in red text.

Details of CAMD-predicted phases for each chemical system

Table S1 below lists all CAMD predictions in the chemical systems selected for experimental synthesis (i.e. Ag-Ca-O, Ag-Li-O, Ca-Pd-O, Ca-O-Ru, Li-O-Ru, and Mg-O-Ru) with stabilities lower than 0.05 eV/atom. The full dataset of CAMD predictions, including those from other chemical systems and those in the selected chemical systems with DFT-predicted stabilities higher than 0.05 eV/atom, can be found in the data repository associated with CAMD at https://figshare.com/articles/dataset/camd2022_tar_gz/19601956.

data_id	stability	chemsys	crystal_sys	space_group	formula

camd_60138	0.000	Ag-Ca-O	cubic	Pm-3n	CaAg3O4
camd_40913	0.000	Ag-Ca-O	cubic	Pm-3m	Ca3AgO4
camd_45666	0.018	Ag-Ca-O	orthorhombic	Pmm2	CaAgO2
camd_98118	0.028	Ag-Ca-O	orthorhombic	Pmmn	CaAg2O3
camd_104952	0.042	Ag-Ca-O	monoclinic	C2/m	Ca3Ag2O5
camd_72720	0.000	Ag-Li-O	cubic	P-43n	LiAg3O4
camd_159085	0.000	Ag-Li-O	tetragonal	P4_2/mmc	LiAgO2
camd_115567	0.000	Ag-Li-O	tetragonal	P4_2/mnm	Li3AgO3
camd_50844	0.033	Ag-Li-O	cubic	Pm-3n	LiAg3O4
camd_61216	0.033	Ag-Li-O	monoclinic	P2_1/c	LiAgO2
camd_72984	0.045	Ag-Li-O	orthorhombic	Pnnm	Li2Ag3O4
camd_47297	0.047	Ag-Li-O	orthorhombic	Pmmn	LiAg2O3
camd_65605	0.000	Ca-O-Pd	orthorhombic	Immm	Ca(PdO2)3
camd_39151	0.007	Ca-O-Pd	orthorhombic	Pnma	CaPdO3
camd_39465	0.024	Ca-O-Pd	monoclinic	P2_1/c	CaPdO3
camd_57163	0.028	Ca-O-Pd	orthorhombic	Pmc2_1	CaPdO3
camd_54742	0.028	Ca-O-Pd	orthorhombic	Pnma	CaPdO3
camd_47329	0.000	Ca-O-Ru	orthorhombic	Pbcn	CaRuO4
camd_47579	0.000	Ca-O-Ru	hexagonal	P6_3	CaRuO3
camd_81624	0.000	Ca-O-Ru	trigonal	R-3	Ca3RuO6
camd_71876	0.002	Ca-O-Ru	monoclinic	P2_1/c	CaRuO3
camd_46822	0.002	Ca-O-Ru	triclinic	P-1	CaRuO3
camd_45199	0.008	Ca-O-Ru	orthorhombic	Pnma	CaRuO3
camd_64161	0.010	Ca-O-Ru	triclinic	P-1	CaRuO4
camd_67393	0.011	Ca-O-Ru	orthorhombic	Pbam	Ca2RuO4
camd_58331	0.013	Ca-O-Ru	trigonal	P-31c	Ca3RuO6
camd_41617	0.013	Ca-O-Ru	monoclinic	P2_1/c	Ca2RuO5
camd_63861	0.015	Ca-O-Ru	monoclinic	P2_1	Ca3RuO6
camd_161552	0.015	Ca-O-Ru	monoclinic	C2/m	Ca(RuO3)2
camd_81842	0.015	Ca-O-Ru	orthorhombic	Pnnm	Ca(RuO3)2
camd_75543	0.016	Ca-O-Ru	tetragonal	P4_2/mnm	Ca(RuO3)2
camd_78781	0.018	Ca-O-Ru	monoclinic	C2/c	Ca3RuO6
camd_129836	0.019	Ca-O-Ru	monoclinic	C2/m	Ca(RuO3)2

camd_80279	0.020	Ca-O-Ru	orthorhombic	Cmmm	Ca2RuO4
camd_53665	0.026	Ca-O-Ru	monoclinic	C2/c	CaRuO4
camd_68522	0.027	Ca-O-Ru	monoclinic	C2/m	Ca2RuO4
camd_75504	0.028	Ca-O-Ru	monoclinic	P2/c	CaRuO4
camd_62825	0.030	Ca-O-Ru	trigonal	R-3c	Ca4RuO6
camd_45861	0.030	Ca-O-Ru	tetragonal	I4_1/amd	CaRuO4
camd_75463	0.031	Ca-O-Ru	orthorhombic	Imma	CaRuO3
camd_71570	0.032	Ca-O-Ru	orthorhombic	Cmcm	CaRuO3
camd_42684	0.032	Ca-O-Ru	orthorhombic	Pbcn	Ca(RuO3)2
camd_50454	0.033	Ca-O-Ru	trigonal	R-3	CaRuO3
camd_108573	0.034	Ca-O-Ru	monoclinic	P2_1/c	CaRuO4
camd_94472	0.035	Ca-O-Ru	orthorhombic	Pccn	Ca2RuO4
camd_54131	0.035	Ca-O-Ru	orthorhombic	Pmmn	CaRuO3
camd_50020	0.036	Ca-O-Ru	monoclinic	P2_1/m	CaRuO3
camd_66178	0.037	Ca-O-Ru	trigonal	R3	Ca3RuO6
camd_56415	0.040	Ca-O-Ru	tetragonal	P4_122	Ca2RuO4
camd_68765	0.040	Ca-O-Ru	orthorhombic	Cmcm	CaRuO4
camd_42292	0.040	Ca-O-Ru	hexagonal	P6_3/mcm	Ca(RuO3)2
camd_100517	0.041	Ca-O-Ru	tetragonal	P4_322	Ca2RuO4
camd_64018	0.046	Ca-O-Ru	orthorhombic	Pnna	CaRuO3
camd_60385	0.049	Ca-O-Ru	tetragonal	I4/mmm	CaRuO3
camd_53058	0.000	Li-O-Ru	tetragonal	P4_322	Li2RuO4
camd_44905	0.000	Li-O-Ru	monoclinic	C2/c	Li4RuO5
camd_45835	0.000	Li-O-Ru	orthorhombic	Pccn	LiRuO3
camd_68313	0.000	Li-O-Ru	monoclinic	C2/c	Li2RuO3
camd_75839	0.000	Li-O-Ru	monoclinic	C2/c	Li3RuO4
camd_43534	0.004	Li-O-Ru	orthorhombic	Fddd	Li2RuO3
camd_62513	0.005	Li-O-Ru	triclinic	P-1	Li4RuO5
camd_130001	0.006	Li-O-Ru	monoclinic	C2/c	Li2RuO3
camd_169141	0.007	Li-O-Ru	orthorhombic	Pnna	LiRuO3
camd_174041	0.009	Li-O-Ru	monoclinic	Cc	Li2RuO3
camd_45405	0.010	Li-O-Ru	monoclinic	C2/m	Li5RuO5
camd_64595	0.011	Li-O-Ru	monoclinic	C2/c	Li2RuO3

camd_171374	0.015	Li-O-Ru	hexagonal	P6_322	LiRuO3
camd_68550	0.016	Li-O-Ru	orthorhombic	Pmc2_1	LiRuO3
camd_67733	0.016	Li-O-Ru	trigonal	R3c	LiRuO3
camd_69320	0.017	Li-O-Ru	monoclinic	P2_1/c	LiRuO3
camd_158919	0.020	Li-O-Ru	tetragonal	P4_122	Li2RuO4
camd_66619	0.020	Li-O-Ru	orthorhombic	Cmce	LiRuO3
camd_83449	0.022	Li-O-Ru	orthorhombic	Pnma	LiRuO3
camd_44914	0.023	Li-O-Ru	tetragonal	I-42d	Li2RuO4
camd_44209	0.024	Li-O-Ru	orthorhombic	Pmmn	Li2RuO3
camd_66137	0.029	Li-O-Ru	orthorhombic	Pbcn	Li2RuO4
camd_114454	0.035	Li-O-Ru	tetragonal	P4_2/mnm	Li3RuO4
camd_85316	0.036	Li-O-Ru	orthorhombic	Pmmn	LiRuO3
camd_109314	0.037	Li-O-Ru	monoclinic	C2/c	Li2RuO4
camd_71055	0.040	Li-O-Ru	orthorhombic	Pmma	LiRuO3
camd_51597	0.042	Li-O-Ru	cubic	Fd-3m	Li2RuO4
camd_42856	0.044	Li-O-Ru	trigonal	R-3c	Li2RuO3
camd_77995	0.046	Li-O-Ru	tetragonal	P4_12_12	Li2RuO4
camd_40616	0.000	Mg-O-Ru	triclinic	P-1	MgRuO4
camd_53651	0.000	Mg-O-Ru	tetragonal	P4_2/mnm	Mg(RuO3)2
camd_78292	0.000	Mg-O-Ru	monoclinic	P2/c	MgRuO4
camd_80073	0.021	Mg-O-Ru	monoclinic	P2_1/c	MgRuO4
camd_65316	0.026	Mg-O-Ru	tetragonal	I4_1md	MgRuO4
camd_56926	0.030	Mg-O-Ru	monoclinic	C2/c	Mg2RuO5
camd_48561	0.032	Mg-O-Ru	orthorhombic	Imma	MgRuO4
camd_57618	0.035	Mg-O-Ru	orthorhombic	Cmmm	MgRuO4

Details of synthesis and characterization

***In situ* XRD:** An HTK-1200N heating stage was used with a PANalytical Empyrean. The milled powders were placed on platinum foil during the scans. Different scanning temperature ranges were used for each system, based on known precursor melting points, or decomposition reactions that reduce oxide into metal or generate unfavoured gas.

Rietveld refinement: Rietveld refinement was performed using GSAS II. The background was estimated by a sixth-order shifted Chebyshev polynomial. Other refined parameters include the

histogram scale factor, phase fractions, sample displacement, lattice constants, atomic site positions, domain size, isotropic microstrain, and instrumental SH/L terms.

4D-STEM: Bragg scattering was localized from 4D-STEM diffraction data using cross-correlative template matching, and the resulting signal was calibrated for origin position, ellipticity, and detector pixel size.

Analysis of LT calcium ruthenate phase

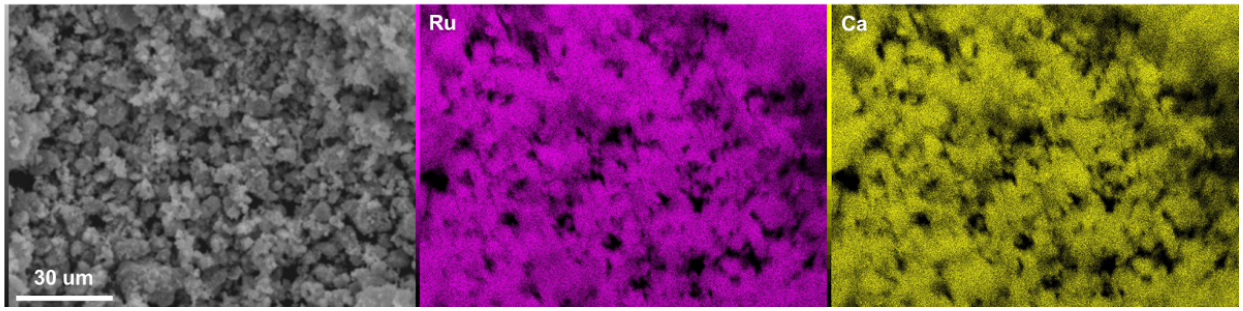

Figure S3: EDS mapping of the isolated LT phase, corresponding to a Ca:Ru ratio of 1.8 for the bulk composition and a macroscopically uniform distribution of Ca. Further TEM characterization (Figure 7) reveals a calcium oxide secondary phase, and confirms a Ca:Ru ratio of 1.6 for the local composition of the LT phase.

Analysis of HT calcium ruthenate phase

In attempts to isolate the high temperature phase, heat treatments were performed first using powder with a larger particle size in order to improve the peak definition. However, the *in situ* phase was not replicated after several attempts. Subsequently, heat treatments were attempted with both the original batch of nanopowder and a new batch of nanopowder. Both of the nanopowder attempts, shown in Figure 8, reproduced the high temperature phase observed in-situ. However, room temperature XRD did not clarify the exact phase composition. Several structures in the calcium ruthenate system match some peaks, but the full peak list cannot be satisfactorily assigned using pre-existing (or predicted) phases. Detailed peak assignment can be found in Table SX. Note that the peak positions of many calcium ruthenate phases match approximately, but often with substantial deviations from both position (>0.5°) and relative intensity (>10%). Phase assignment is further complicated by the significant overlap of many mixed calcium ruthenate oxides and the possibility of non-equilibrium effects introduced by quenching. Expanding the search to precursors and their derivatives does not resolve the poor fit, and some peaks remain unmatched entirely. Certain features of the spectrum are highly unusual, such as the multiple double peaks around 18 and 19°; one set of these peaks can be associated with a calcium-rich $Ca_{2.83}RuO_{4.83}$ phase, but not both. The most likely resolution is that multiple mixed phases are present and severely distorted by the nanoscale nature of the powder, but the possibility of an unknown low symmetry phase cannot be discounted because the composition can not be satisfactorily resolved.

Characterization of this high temperature powder via EDS confirms that the quenched powder is multiphase, containing at least two phases with distinct Ca concentrations as well as small amounts of localized impurities such as Al and Na (Figure 8b and c). These impurities do not appear in sufficient quantities to explain the major unassigned peaks in the XRD patterns.

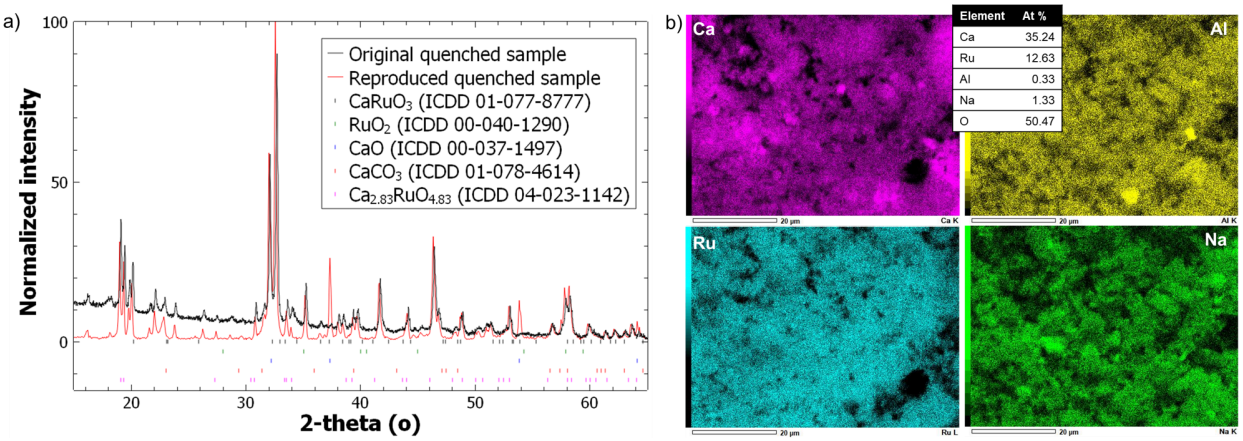

Figure S4: a) Room temperature XRD of high temperature phase obtained and reproduced by quench experiments and b) EDS mapping indicating multiphase nature with average composition reported.

Table S2: Detailed assignment of major peaks in the room temperature XRD diffraction pattern of the high temperature (HT) Ca-Ru-O phase.

Pos. [°2θ]	d-spacing [Å]	Rel. Int. [%]	PDF peak match	PDF intensity	Matched by
16.1255	5.49204	2.14			
18.157	4.88188	1.54			04-011-8727
18.9856	4.67065	29.8	18.947	47.9	01-073-8394 (Ca(OH)2) Requires 100 peak at 36.487
19.3312	4.58792	21.43	19.340	100	04-023-1142 (Ca2.83RuO4) Requires an additional 92.4 intensity peak at 19.095
19.7655	4.48808	7.84			04-014-5351
20.0231	4.4309	15.09	19.999 20.140	0.1 46.6	04-014-5351 (CaRuO3) 04-014-7728 (Ca(OH)2)

Pos. [°2θ]	d-spacing [Å]	Rel. Int. [%]	PDF peak match	PDF intensity	Matched by
					requires 100 peak at 36.36
21.5861	4.11347	2.24			04-011-8727
22.0397	4.02984	7.7			04-012-6012
22.7128	3.91191	3.55			04-014-5351
22.8538	3.8881	3.53			04-014-5351
23.7696	3.74032	3.97			
26.2427	3.39317	2.84			
27.3775	3.25505	2.01			04-023-1142, 04-011-8727, 04-012-6012
28.6379	3.11459	1.26			
29.5954	3.01596	0.9			04-012-6012
30.7906	2.90157	6.85			04-023-1142, 01-073-8394
32.0126	2.79354	50.73	32.347 32.311 31.874 32.304	26.6 41.1 100 100	04-014-5351 (CaRuO3, added manually) 04-005-4398 (CaO, requires 100 peak at 37.481) 04-014-3870 (RuO2, requires a 47 peak at 36.970) 04-012-6012 (Ca2RuO4, requires 45.6 peak at 24.259 where there isn't one)
32.5836	2.74587	100	32.731 32.569 32.591	100 100 38.6	04-014-5351 (CaRuO3) 04-011-8727 (Ca3Ru2O7, requires a

Pos. [°2θ]	d-spacing [Å]	Rel. Int. [%]	PDF peak match	PDF intensity	Matched by
					34.6 peak at 32.395) 04-012-6012 (Ca2RuO4, requires a 100 peak at 32.304)
33.5375	2.66992	6.25	33.03	25.0	04-014-5351 (CaRuO3, added manually) 04-023-1142, 04-011-8727
33.9398	2.63919	3.44			04-023-1142, 04-011-8727, 04-012-6012
35.144	2.55147	13.7			Unmatched
36.4566	2.46256	1.4	36.487	100	01-073-8394 (Ca(OH)2) 04-014-5351, 04-012-6012, 04-014-7728,
37.3363	2.40653	27.27	37.481 37.356 37.477	100 2.0 1.1	04-005-4398 (CaO, requires a 50.9 peak at 54.048) 04-011-8727 (Ca3Ru2O7, requires an identical 2 peak at 38.149 and a 30.8 peak at 18.101) 04-012-6012 (Ca2RuO4, requires two additional 1 and 0.4 peaks at 37.049 and 37.832)
38.0115	2.36533	5.25	38.088	1.6	04-012-6012 (Ca2RuO4, see above for additional requirements)
38.424	2.34088	3.96			04-014-5351,

Pos. [°2θ]	d-spacing [Å]	Rel. Int. [%]	PDF peak match	PDF intensity	Matched by
					04-011-8727, 01-073-8394
39.2936	2.29105	6.93			04-023-1142, 04-011-8727
39.65	2.27128	6.3			04-012-6012
41.6205	2.16818	19.94	41.523 41.626	4.4 0.5	04-014-3870 (RuO2, requires 100 peak at 31.874 and a 47.0 peak at 36.970) 04-011-8727 (Ca3Ru2O7, see above for requirements)
44.0342	2.05477	6.88			04-023-1142
44.6185	2.02921	0.65			04-012-6012
45.2421	2.00268	1.25			04-012-6012
46.3277	1.95825	29.78	46.035 46.315	26.9 16.2	04-023-1142 (Ca2.83RuO4.83, see above for additional requirements) 04-011-8727 (Ca3Ru2O7, requires 28.8 peak at 47.136)
46.7552	1.94133	6.61			04-014-5351, 04-011-8727
48.2326	1.88526	1.78			04-014-5351, 04-023-1142, 04-011-8727, 04-012-6012
48.7665	1.86586	7.15			
50.1654	1.81706	1.67			04-023-1142, 01-073-8394

Pos. [°2θ]	d-spacing [Å]	Rel. Int. [%]	PDF peak match	PDF intensity	Matched by
50.9441	1.7911	3.3			04-023-1142, 04-011-8727
51.2901	1.77983	4.47			04-014-5351
52.6177	1.738	2.78			04-014-5351, 04-023-1142, 04-012-6012
52.9722	1.7272	12.43	53.177. 52.974 52.921/52.719 52.754 53.177	23.4 15.4 0.5/6.8 0.4 23.4	04-014-5351 (Ca(OH)2, requires 100 peak at 36.360) 04-023-1142 (Ca2.83RuO4.83, requires 15.1 peak at 52.467 and 13.0 peak at 52.059) 04-011-8727 (Ca3Ru2O7) 04-012-6012 (Ca2RuO4) 04-014-7728 (Ca(OH)2)
53.8488	1.70114	13.94	54.048 53.804 53.931 53.361	50.9 1.5 3.4 8.4	04-005-4398 (CaO) 04-014-5351 (CaRuO3) 04-011-8727 (Ca3Ru2O7) 04-012-6012 (Ca2RuO4)
56.6635	1.62313	4.08			04-023-1142
57.5089	1.60126	4.77			04-014-7728
57.8141	1.59353	16.77	57.936 57.894 57.974/57.428/ 57.083	14.6 13.4 13.5/11.7/11. 3	04-014-5351 (CaRuO3) 04-011-8727 (Ca3Ru2O7) 04-012-6012 (Ca2RuO4)
58.1831	1.58431	17.83	58.052 58.225	4.8 13.4	04-023-1142 (Ca2.83RuO4.83)

Pos. [°2θ]	d-spacing [Å]	Rel. Int. [%]	PDF peak match	PDF intensity	Matched by
					04-011-8727 (Ca3Ru2O7)
59.8755	1.5435	3.73			04-023-1142, 04-012-6012
60.2847	1.534	1.92			04-023-1142
61.3072	1.51085	2.91			04-014-5351, 04-011-8727
62.1079	1.49328	3.24			04-014-7728
62.9749	1.47479	2.44			04-011-8727, 04-012-6012
63.6116	1.46155	5.68			04-014-3870, 04-023-1142, 04-011-8727, 04-012-6012
64.1654	1.45027	5.68			04-005-4398, 04-014-5351, 04-023-1142, 04-011-8727, 04-012-6012

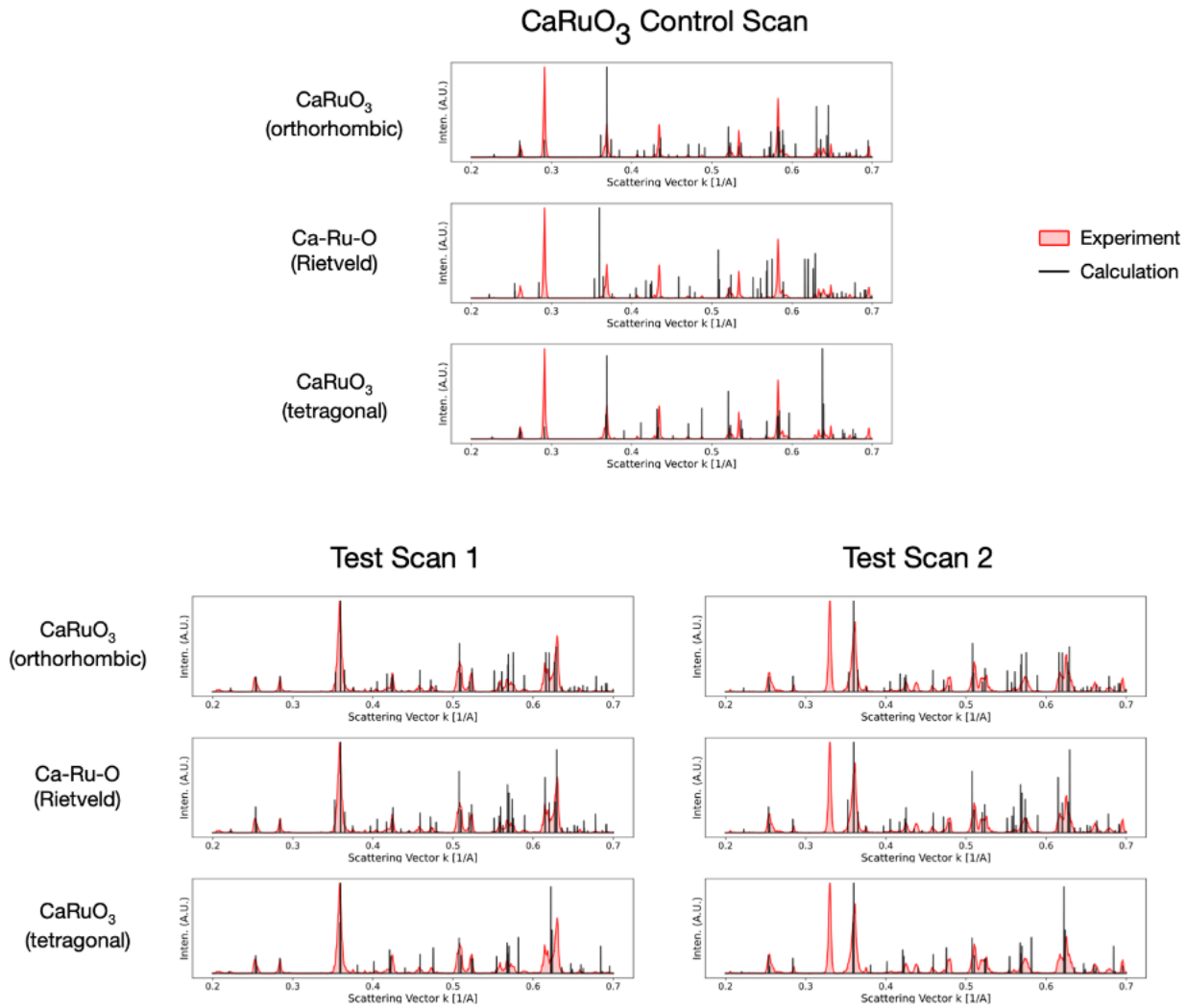

Figure S5: Bragg scattering profiles isolated from 4D-STEM scans of the standard sample and two scans of the LT phase (test scans), compared to computed scattering for standard orthorhombic $CaRuO_3$, to the Rietveld refined Ca-Ru-O structure, and to a simplified $CaRuO_3$ structure in which the a and c lattice parameters have been replaced by their mean, resulting in a tetragonal structure. The standard sample is compared to an unmodified standard $CaRuO_3$ structure, while the scans of the LT phase are compared to $CaRuO_3$ with its cell expanded isotropically by 2.55%.

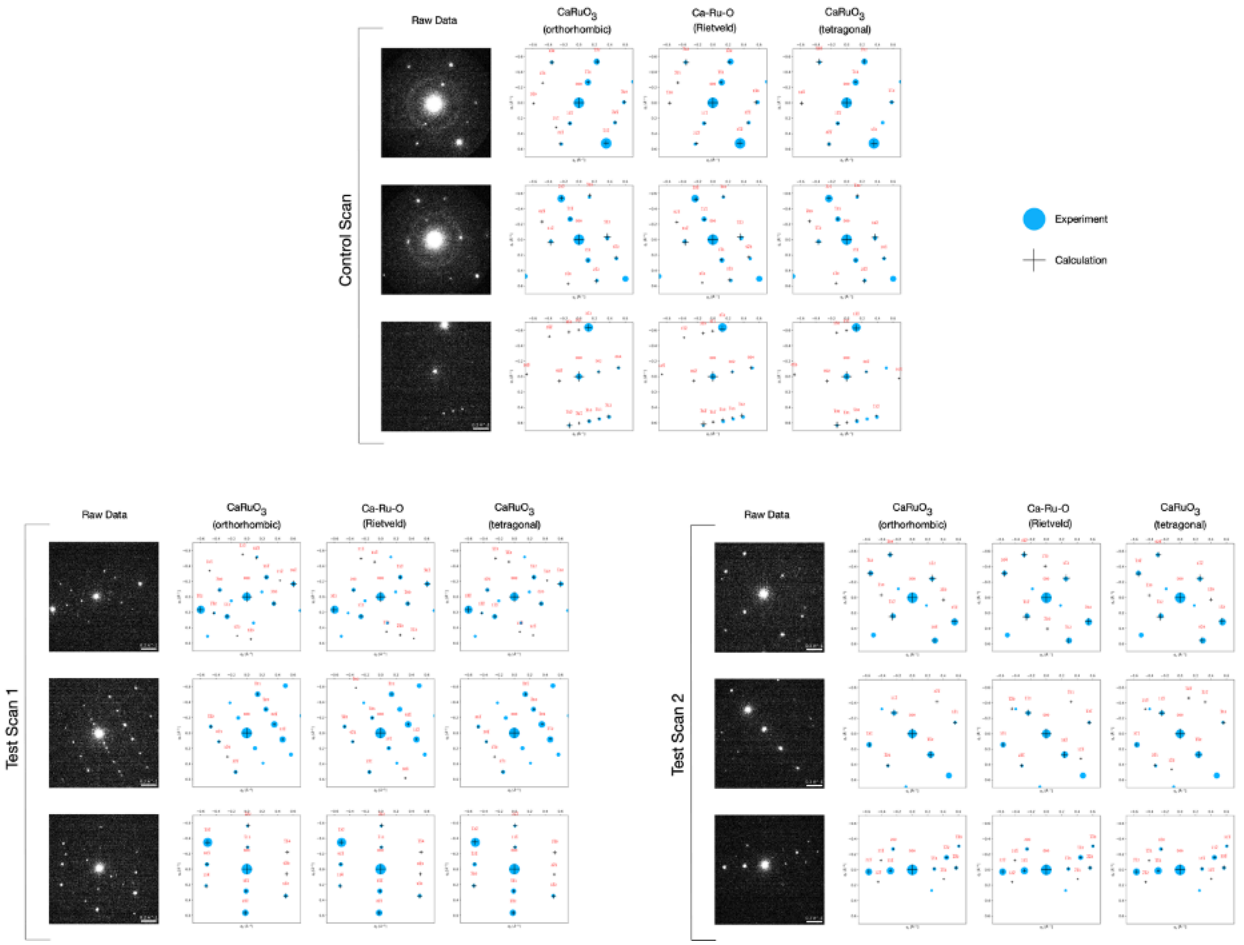

Figure S6: Two-dimensional pattern matching between standard orthorhombic $CaRuO_3$, simplified tetragonal $CaRuO_3$, and the Rietveld refined LT phase structure versus Bragg signal isolated from 4D-STEM scans of the standard sample and two scans of the LT phase (test scans). The $CaRuO_3$ structure was expanded isotropically by 2.55% in the matches to the datasets of the LT phase, and is unmodified in the matches to the standard dataset. The structures are quite similar, leading to similar matches to the data.

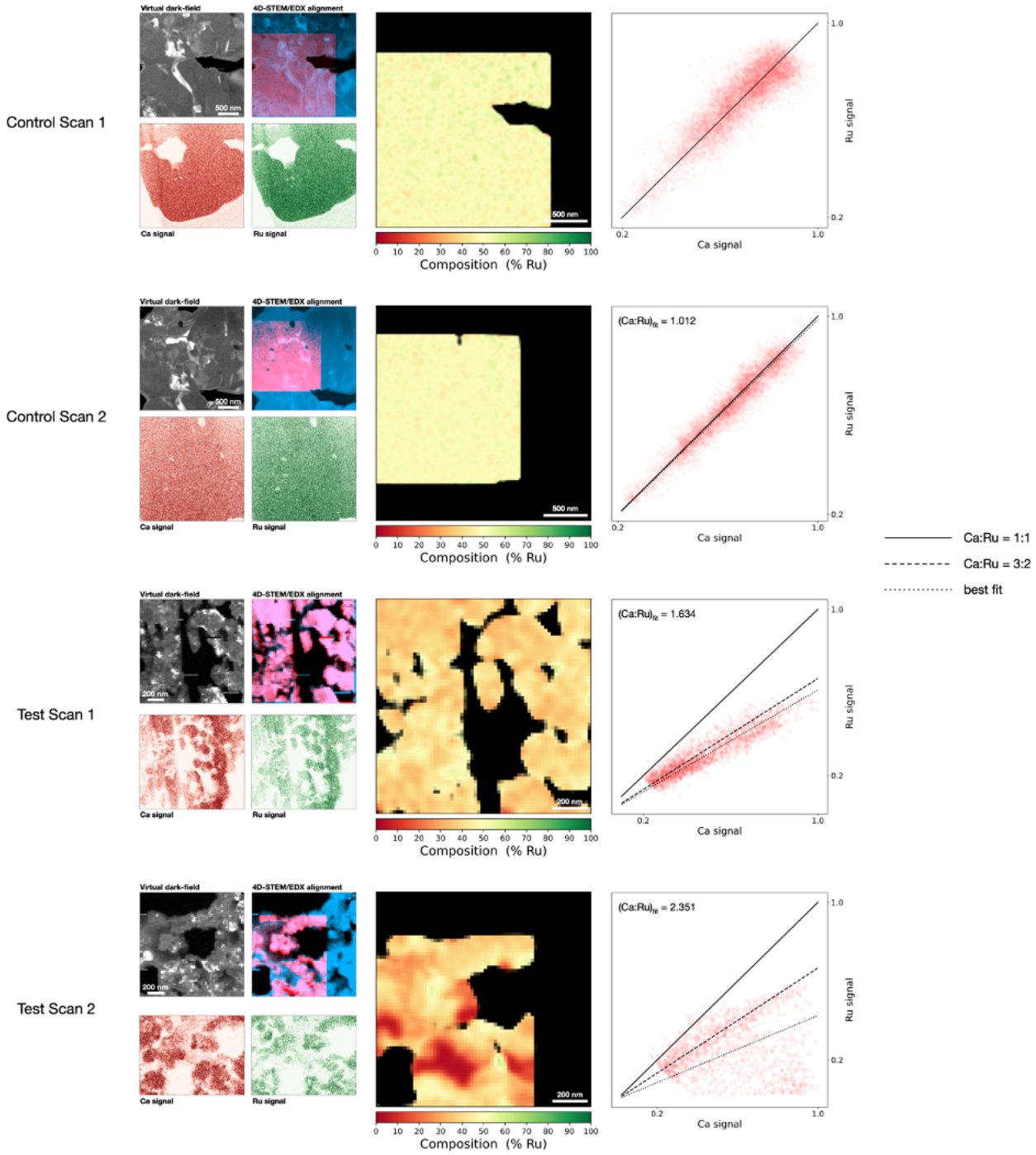

Figure S7: Alignment of EDX- and 4D- STEM for two standard scans and two scans of the LT phase. We solved for the affine transformation which best aligns the combined EDX signal to a contrast inverted virtual bright-field signal. The alignment images show the bright-field in the blue channel and the transformed EDX signal in the red channel. The scaling ratio (k-factor) between the Ca and Ru signals was extracted using the first standard scan and assuming a Ca:Ru atomic ratio of 1:1. The best fit line to the composition scatter plot from the second standard scan yields a Ca:Ru ratio of 1.012.

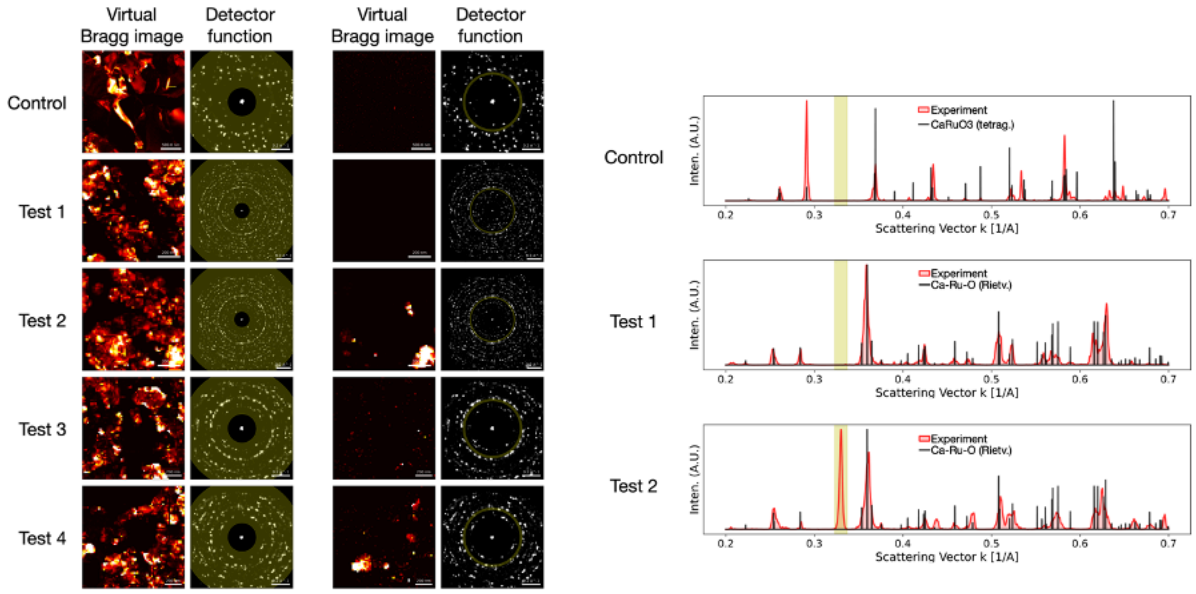

Figure S8: Virtual Bragg images of all high-angle Bragg scattering and of the Bragg scattering in the window 0.330 ± 0.007 Å^{-1} spanning a calcium oxide peak. The signal used to compute these images is the localized Bragg scattering signal, with positions and intensities determined by cross correlating the STEM vacuum probe with each diffraction pattern to localize Bragg reflections of the probe. The detector functions shown in yellow indicate the regions of diffraction space Bragg signal must fall within to be summed when computing the corresponding images. The narrow detector function is also shown overlaid with 1D scattering profiles for several scans, with the oxide peak clearly visible in the profile for test scan 2 of the LT phase. No calcium oxide peak was found in any of the standard scans. The peak was present in some but not all of the test scans of the LT phase, with maps of the calcium oxide grains visible in the corresponding virtual Bragg images.

Details of SQUID measurements

Magnetization was measured down to 5K using a superconducting quantum interference device (Quantum Design SQUID VSM magnetometer). The measurements were taken via SQUID against both temperature and magnetic field. For the field-cooled (FC) measurements, the sample was cooled to 5K under an applied 3 kOe field; then the field was removed and the sample was warmed to room temperature under a 100G field while magnetization was measured. For zero field-cooled (ZFC) measurements, the same procedure was repeated, except no field was applied during the cooling step. Magnetization as a function of applied field was measured by cooling with (ZFC) or without (FC) applied field to 5K, removing the applied field, then applying the maximum field and cycling down and back up, collecting magnetization data.

Additional XRD patterns

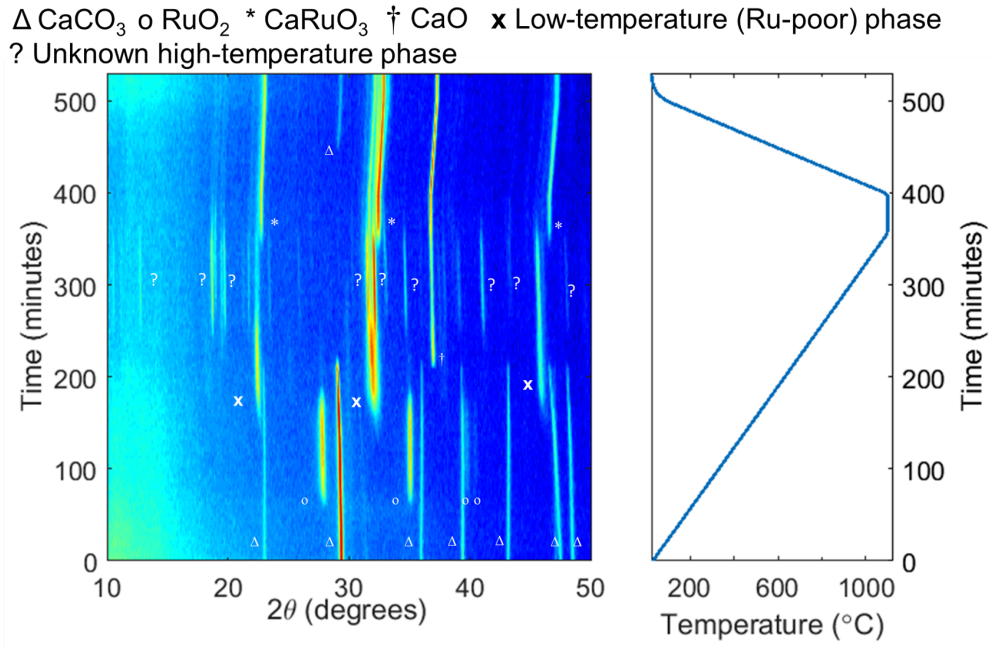

Figure S9: provides the annealing and cooling data which demonstrate the collapse of the metastable phase into $CaRuO_3$ and excess CaO.

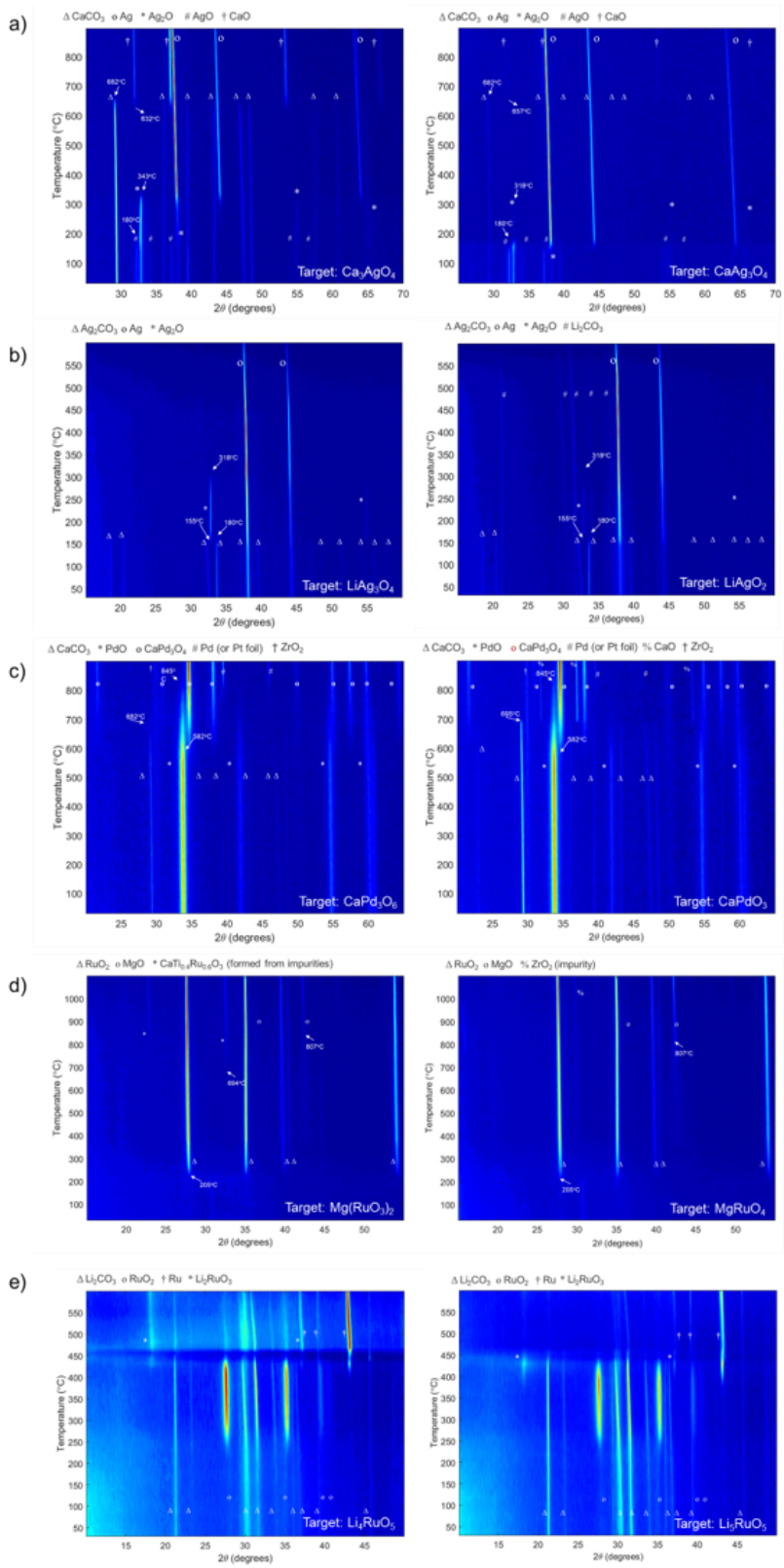

Figure S10: In-situ XRD results for a) Ca-Ag-O, b) Li-Ag-O, c) Ca-Pd-O, d) Mg-Ru-O, e) Li-Ru-O.